Efficiency assessment of modular multilevel converters for battery electric vehicles

Quraan, Mahran; Tricoli, Pietro; D'Arco, Salvatore; Piegari, Luigi

DOI:
10.1109/TPEL.2016.2557579

License:
Other (please specify with Rights Statement)

Document Version
Peer reviewed version

Citation for published version (Harvard):
Quraan, M, Tricoli, P, D'Arco, S & Piegari, L 2017, 'Efficiency assessment of modular multilevel converters for battery electric vehicles', *IEEE Transactions on Power Electronics*, vol. 32, no. 3, pp. 2041 - 2051. https://doi.org/10.1109/TPEL.2016.2557579

Efficiency Assessment of Modular Multilevel Converters for Battery Electric Vehicles

M. Quraan *, P. Tricoli *, *member*, *IEEE,* S. D'Arco †, L. Piegari +, *senior member, IEEE*
* School of Electronic, Electrical and Systems Engineering, University of Birmingham, UK
†SINTEF Energy Research, Norway,
+DEIB - Politecnico di Milano, Italy,

***Abstract*—This paper evaluates the performance of modular multilevel converters with integrated battery cells when used as traction drives for battery electric vehicles. In this topology, individual battery cells are connected to the dc-link of the converter submodules, allowing the highest flexibility for the discharge and recharge. The traditional battery management system of battery electric vehicles is replaced by the control of the converter, which individually balances all the cells. The performance of the converter as a traction drive is assessed in terms of torque-speed characteristic and power loss for the full frequency range, including field weakening. Conduction and switching losses for the modular multilevel converter are calculated using a simplified model, based on the data sheet of power devices. The performance of the modular multilevel converter is then compared with a traditional two-level converter. The loss model of the modular multilevel converter is finally validated by experimental tests on a small-scale prototype of traction drive.**

***Index Terms*—Battery electric vehicles, modular multilevel converters, state of charge balancing, traction drives, switching losses, conduction losses**.

I. Introduction

In recent years a wide diffusion of battery electrical vehicles (BEVs) is taking place, although customers have still significant concerns regarding limited battery life, reduced vehicle range and long recharge time. For this reason, novel types of batteries have been designed over the last years to improve their performance. The battery cells for BEVs are normally series connected to meet the voltage requirements of the traction converter [1]. However, voltage imbalance between the cells appears when the battery is charged or discharged several times, because of the differences in leakage currents and chemical characteristics of battery cells; this causes progressive damage of battery cells and reduction of their service life time [2]. In order to minimise this effect, a second dc-dc converter is used for cell balancing and controlled by the battery management system (BMS). For some BEVs, a third converter is used on board for cell recharging from the ac utility grid. The functions of these three converters could be brought together in one converter only, as shown in [3]-[5]. This converter is a special type of modular multilevel converter (MMC) without voltage supply on the dc busbars, in which each submodule (SM) is constituted by an H-bridge converter connected to one battery cell. This converter includes a BMS [4] and can be successfully used to drive a traction motor [3] and to recharge the battery cells both from single-phase and three-phase grids [5]. Since the THD of the output voltage is very low, torque ripple is negligible and motor efficiency is higher than that under two-level inverter-fed operations [6], [7]. Additionally, the reliability of MMC is very high if compared with two-level inverters [8].

One of the main drawbacks of MMCs for low voltage applications is the increased conduction losses, if compared with traditional inverters due to the high number of devices conducting in series. This is mitigated by the lower switching losses and by an appropriate choice of the devices. In order to assess the suitability of MMCs for traction drives, this paper undertakes a thorough analysis of the power losses in the different operating regions of the BEV. This analysis shows that, using a proper modulation strategy, the switching losses of the MMC are much lower than those of traditional inverters and the global efficiency is comparable and even higher in some cases. The comparison does not consider the power losses in the cell balancing converter used for the traditional inverter, so the MMC is penalised. Moreover, the global efficiency remains almost constant also at low speed/voltage and light loads, whereas the efficiency of traditional inverters drastically decreases. When the speed and the load of the traction drive is reduced for most of the time, like the case of urban cycles, MMC traction drives operate with higher efficiency and, consequently, the vehicle range increases.

The paper is organised as follows. Section II reviews the MMC structure and its principle of operations; section III describes the proposed control strategy that includes the cell balancing function; section IV describes the proposed method for the calculation of power losses for the MMC; section V presents the simulation results for the sample case of the new European driving cycle (NEDC) and the comparison between the MMC and the 2-level inverter; section VI validates with experimental results the proposed method for the calculation of power losses and the motor drive performance over the NEDC.

II. Converter Topology and Operating Principle

A schematic diagram of the proposed MMC is shown in Fig. 1. The power converter drives a traction motor, which is assumed to be a three-phase induction machine. Each phase-leg of the power converter is composed by two arms consisting of n cascaded SMs. The converter arms are connected by means of two uncoupled buffer inductors, to limit the circulating currents due to voltage mismatch between the phase-legs [9], [10]. Each SM contains a bidirectional half-bridge converter and a battery cell. The cell voltage, v_{cell}, depends on its SOC and

varies between 3.2 V and 4.2 V. Since the maximum operating voltage of each SM is the cell voltage, low voltage MosFETs can be used to reduce conduction and switching losses.

All the quantities referred to a phase are denoted with the subscripts *a*, *b*, *c* or with the subscript *k* when instead reference is made to a generic phase. Quantities associated to the top and bottom arms are indicated with the subscripts *t* and *b*, respectively.

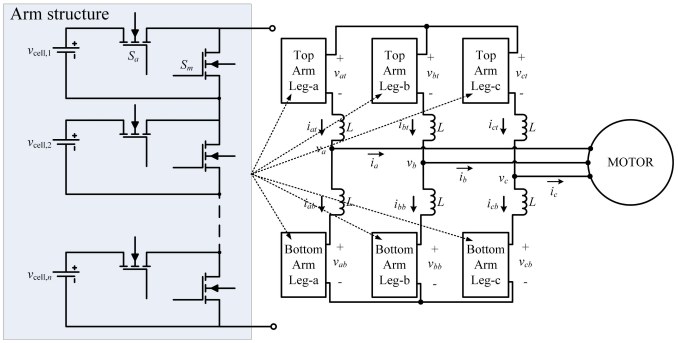

Fig. 1: Schematic diagram of the proposed MMC.

The number *n* of active SMs for each phase-leg is constant, resulting in a nearly constant sum voltage. In order to achieve this, the two arms of the same phase-leg are controlled complementarily, i.e. $n_{kt} + n_{kb} = n$ [11].

The arm currents flow through the battery cells of the active SMs and either charge or discharge the cells depending on their direction. According to [11], the arm currents are defined as:

$$i_{kt} = i_{cir,k} + \frac{1}{2} i_k; \quad i_{kb} = i_{cir,k} - \frac{1}{2} i_k, \tag{1}$$

where $i_{cir,k}$ is circulating current of the *k*-th phase. The arm voltages can be expressed as:

$$\begin{aligned} v_{kt} &= \frac{n v_{\text{cell}}}{2} - v_k - \frac{L}{2}\frac{di_k}{dt} - \underbrace{L\frac{di_{cir,k}}{dt}}_{v_{L,cir,k}}; \\ v_{kb} &= \frac{n v_{\text{cell}}}{2} + v_k + \frac{L}{2}\frac{di_k}{dt} - \underbrace{L\frac{di_{cir,k}}{dt}}_{v_{L,cir,k}}, \end{aligned} \tag{2}$$

where v_k is the voltage of the *k*-th phase, *L* is the buffer inductance, and $v_{L,cir,k}$ is the voltage drop across *L* due to $i_{cir,k}$.

The modulation technique of the converter is based on the carrier disposition with third harmonic injection sinusoidal PWM (THI-SPWM). The third harmonic injection effectively reduces the number of required SMs by 13.5%, leading to a reduction in converter size, cost, and losses. The modulation index, *m*, in the hypothesis of balanced cells is defined as [12], [13]:

$$m = \frac{2V_m}{n v_{cell}}; \quad 0 \le m \le \frac{2}{\sqrt{3}}, \tag{3}$$

where V_m is the amplitude value of phase voltage output of the converter.

The configurations based on two level inverters typically include a BMS to balance the battery cells. The physical implementation of a BMS involves the presence of additional hardware components. However, in the proposed configuration with MMC this balancing function is embedded in the converter. Thus, a fair comparison between configurations in a cost, volume or weight perspective should not be limited only to the converters but account also for any added BMS. A component count and a qualitative cost assessment between the proposed MMC configuration and alternative configurations with a two-level inverter and different active BMS topologies is summarized in Table I [8].

TABLE I
COMPARISON OF THE PROPOSED MMC WITH THE TWO-LEVEL INVERTER FOR DIFFERENT ACTIVE BMSS [8].

Traction drive	Active BMS topology	L	C	SW	D	IC	Cost
Two-level inverter	Switched Capacitor	0	$N-1$	$2N+6$	6	0	++
	Double-Tiered Switched Capacitor	0	$(3N-3)/2$	$2N+6$	6	0	++
	Single Switched Capacitor	0	1	$N+11$	6	0	+++
	Modularized Switched Capacitor	0	$N-m$	$2N+6$	6	0	++
	Multi Switched Inductor	$N-1$	0	$2N+4$	6	0	++
	Single Switched Inductor	1	0	$2N+6$	$2N+4$	0	++
	Single Winding Transformer	2	0	$N+12$	6	1	+
	Multi-Winding Transformer	$N+1$	0	8	6	1	+
	Buck-Boost Converter	1	1	$N+13$	6	0	++
	Ćuk Converter	$2N-2$	$N-1$	$2N+4$	6	0	++
	Flyback Converter	$2N$	1	$2N+6$	6	N	+
	Ramp Converter	$N/2$	N	$N+6$	$N+6$	1	+
MMC	MMC	6	0	$2N$	0	0	++

L: Inductor, C: Capacitor, SW: Switch, D: Diode, IC: Iron Core, *N*: number of cells, m: number of modules, +++: Excellent, ++: Good, +: Satisfactory.

III. CONTROL STRATEGY OF THE CONVERTER

The drive control presents three main functional blocks: the traction drive control, the arm balancing control and the cell balancing control.

The traction drive control calculates the references for the power converter to enable variable speed operations of the induction motor. This control is based on a standard vector control and no further details will be provided in this paper. The arm balancing control uses the circulating currents to balance the electrochemical energy stored across the phases and, within each phase, across the top and bottom arm. The balance of energy stored across the phases is achieved by balancing the average state of charge (SOC) of all the cells belonging to each phase. The energy balance across the top and bottom arm of a phase is achieved by balancing the average state of charge of all the cells belonging to the top arm and all the cells belonging to the bottom arm. The cell balancing control activates the SMs with the logic appropriate to balance the energy stored in each individual cell within an arm. The details of the implementation of these two functional blocks are described in the following subsections.

A. Arm Balancing Control

The block diagram of the arm balancing control is shown in Fig. 2. The circulating currents are controlled to include a dc component, $i_{cir,dc,k}$ and a fundamental component $i_{cir,1,k}$, having amplitude $i_{m,cir,k}$ and phase angle γ_k:

$$\begin{aligned} &i_{cir,k} = i_{cir,dc,k} + i_{m,cir,k}\sin(\theta_k);\\ &\begin{bmatrix}\theta_a & \theta_b & \theta_c\end{bmatrix}^T = \begin{bmatrix}\omega t+\gamma_a & \omega t+\gamma_b-2\pi/3 & \omega t+\gamma_c+2\pi/3\end{bmatrix}^T. \end{aligned} \tag{4}$$

The balance between the phases is achieved by controlling the total active power generated by the battery cell in each phase, p_k^{Σ}. The balance between top and bottom arm within a phase is instead achieved by controlling the difference of the active powers generated by the battery cells of the top and bottom arms of that phase, p_k^{Δ}. Ignoring the device power losses and according to [8], p_k^{Σ} and p_k^{Δ} can be calculated as:

$$\begin{aligned} p_k^{\Sigma} &= 2n v_{\text{cell}} Q \frac{d\overline{\text{SOC}}_k}{dt} \cong \\ &\cong n v_{\text{cell}} i_{cir,dc,k} - \frac{1}{2} V_m I_m \cos\varphi; \\ p_k^{\Delta} &= n v_{\text{cell}} Q \frac{d}{dt}\left(\overline{\text{SOC}}_{kt} - \overline{\text{SOC}}_{kb}\right) \cong \\ &\cong -V_m c_k; \quad c_k = i_{m,cir,k}\cos\gamma_k, \end{aligned} \tag{5}$$

where Q is the cell capacity, $\overline{\text{SOC}}$ is the moving average of the SOC, $\cos\varphi$ is the load power factor. The relations in (5) indicate that the energy balance across the phases can be controlled by means of $i_{cir,dc,k}$, while the balance across top and bottom arms can be controlled by means of $i_{cir,1,k}$. With this choice of the components of the circulating current, the two controls are decoupled and can be implemented in two separate regulators. The reference for the dc components of the circulated currents can be obtained directly from PI regulators; the reference for the first harmonic component can be calculated from the formulae given in Appendix A1.

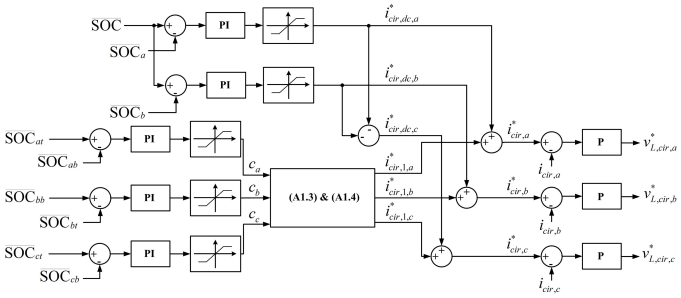

Fig. 2: Block diagram of circulating current controller.

The control system is implemented digitally in a field programmable gate array (FPGA), so the block diagram in Fig. 2 needs to be converted into a the discrete-time model as shown in Appendix A2.

B. Cell Balancing Control

The cell balancing algorithm is based on the concept that, when the arm current is positive according to Fig. 1, the cells of the active SMs are recharged and their SOC increases and vice versa when the arm current is negative. This approach ensures a step-by-step equalization of the SOCs of the cells belonging to the same arm. The algorithm estimates the SOCs and sorts the cells in each arm in descending order on the basis of their SOC. Due to the slow variation of SOC, this control loop can be executed as low priority and has a running time of 1 ms. The SOC of each cell is estimated by the Coulomb counting approach. If the arm current is positive, the cells with the lowest SOCs are activated; if the arm current is negative, the cells with the highest SOCs are activated [14]-[16].

IV. METHODOLOGY FOR THE CALCULATION OF CONVERTER LOSSES

The power losses of the converter devices can be divided into conduction losses, P_c, and switching losses, P_{sw} and separately analyzed in the following subsections. For simplicity, other losses like gate drivers, magnetics and auxiliaries are not considered in this section.

A. Conduction Losses

The instantaneous conduction losses for each power MosFET can be calculated using the equivalent drain-source on-state resistance $R_{ds,on}$ [17]:

$$p_{c,M} = v_{ds} i_d = R_{ds,on} i_d^2, \tag{6}$$

where v_{ds} and i_d are the drain-source voltage and the drain current of the MosFET, respectively.

Each SM includes two power MosFETs but only one is on at the same time, if dead-time is not considered. Thus, the number of MosFETs conducting in each arm is equal to n and the instantaneous conduction losses can be expressed as:

$$\begin{aligned} p_{c,kt} &= nR_{ds,on} i_{kt}^2 = n R_{ds,on}\left(i_{cir,k} + \frac{1}{2} i_k\right)^2; \\ p_{c,kb} &= nR_{ds,on} i_{kb}^2 = n R_{ds,on}\left(i_{cir,k} - \frac{1}{2} i_k\right)^2. \end{aligned} \tag{7}$$

Thus the losses in each phase leg result in:

$$p_{c,k} = p_{c,kt} + p_{c,kb} = 2nR_{ds,on}\left(i_{cir,k}^2 + \frac{1}{4}i_k^2\right). \quad (8)$$

Since the circulating current is normally few percent of the nominal current and is present only during cell balancing, its contribution to the conduction losses is negligible. Therefore, (8) can be approximated by:

$$p_{c,k} = \frac{1}{2}nR_{ds,on}i_k^2. \quad (9)$$

Assuming that the load current has only the fundamental component and is balanced, the total MMC conduction losses, P_c, can be calculated as:

$$P_c = \frac{3}{T}\int_0^T p_{c,k}\,dt = \frac{3}{4}nI_m^2R_{ds,on}, \quad (10)$$

where I_m is the amplitude value of phase current output of the converter. Therefore, the total MMC conduction losses are independent from the modulation index and the load power factor.

B. Switching Losses

For this calculation, a linear approximation of the MosFET voltage and current during the switching process has been assumed. Thus, turn-on and turn-off switching energy losses for a single MosFET $E_{sw,on}$, $E_{sw,off}$, are given by [17]:

$$\begin{aligned} E_{sw,on} &= \frac{1}{2}v_{cell}\,i_d\,(t_{ri} + t_{fv}) = \frac{1}{2}v_{cell}\,i_d\,t_{on}; \\ E_{sw,off} &= \frac{1}{2}v_{cell}\,i_d\,(t_{fi} + t_{rv}) = \frac{1}{2}v_{cell}\,i_d\,t_{off}, \end{aligned} \quad (11)$$

where t_{ri} and t_{fi} are the current rise and fall times, t_{rv} and t_{fv} are the voltage rise and fall times. In (11), v_{cell} and i_d are considered at the initial instant of switching. Each change of the conduction state of a cell corresponds to the turn-on of one MosFET and the simultaneous turn-off of the other MosFET of the same SM. Thus, at each change of the conduction state of the SM, the energy dissipated is equal to:

$$E_{sw} = E_{sw,on} + E_{sw,off} = \frac{1}{2}v_{cell}\,i_d\,(t_{on} + t_{off}). \quad (12)$$

If for simplicity the switching events are supposed to be regularly spaced, each arm is switched at T_{sw}, $2T_{sw}$, $3T_{sw}$ … zT_{sw}, where z is the total number of switching events in a fundamental period, T, and it is given by:

$$z = \frac{T}{T_{sw}} = \frac{f_{sw}}{f}. \quad (13)$$

The total number of switching events is split across the SMs of the arm, so that:

$$z = \sum_{h=1}^{n} z_h, \quad (14)$$

where z_h is the number of PWM pulses of the h-th SM.

Fig. 3 shows an example of waveforms for the currents flowing into the SMs of a converter arm in the case of 4 SMs/arm.

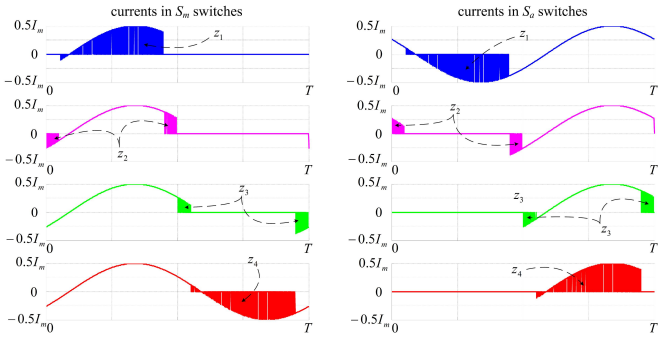

Fig. 3: Currents flowing into all switches within one arm (n = 4).

Suppose that the h-th SM is switching at $z_{h1}T_{sw}$, $z_{h2}T_{sw}$, $z_{h3}T_{sw}$ …, $z_{hzh}T_{sw}$ where z_{h1}, z_{h2}, z_{h3} …, z_{hzh} are in general unequal integer numbers. As long as THI-SPWM scheme is used, the others $n - 1$ SMs will remain in a constant switching state. In this case, the h-th SM currents at instant of switching are:

$$\left\{\begin{array}{l} \frac{1}{2}I_m\left|\sin(z_{h1}\omega T_{sw})\right| \\ \frac{1}{2}I_m\left|\sin(z_{h2}\omega T_{sw})\right| \\ \frac{1}{2}I_m\left|\sin(z_{h3}\omega T_{sw})\right| \\ \vdots \\ \frac{1}{2}I_m\left|\sin(z_{hz_h}\omega T_{sw})\right| \end{array}\right\} \quad (15)$$

As a result, the switching energy dissipated in a SM, $E_{sw,h}$, during a fundamental period can be expressed as:

$$E_{sw,h} = E_{sw}^*\sum_{j=1}^{z_h}\left|\sin(z_{hj}\omega T_{sw})\right|;\ E_{sw}^* = \frac{1}{2}v_{\text{cell}}I_m(t_{on} + t_{off}), \quad (16)$$

and the switching energy dissipated in an arm, $E_{sw,arm}$, during a fundamental period can be expressed as:

$$\begin{aligned} E_{sw,arm} &= E_{sw}^*\sum_{j=1}^{z_1}\left|\sin(z_{1j}\omega T_{sw})\right| + E_{sw}^*\sum_{j=1}^{z_2}\left|\sin(z_{2j}\omega T_{sw})\right| + \\ &+ \cdots + E_{sw}^*\sum_{j=1}^{z_n}\left|\sin(z_{nj}\omega T_{sw})\right| \\ &= E_{sw}^*\sum_{i=1}^{z}\left|\sin(i\omega T_{sw})\right| = E_{sw}^*\sum_{i=1}^{z}\left|\sin(2\pi i/z)\right| = \\ &= 2E_{sw}^*\cot(\pi/z) \approx E_{sw}^*\left(\frac{2z}{\pi} - \frac{2\pi}{3z}\right). \end{aligned} \quad (17)$$

Finally, the power dissipated in the converter due to switching losses can be calculated as:

$$P_{sw} = 6fE_{sw,arm} \approx 4E_{sw}^*\left(\frac{3f_{sw}}{\pi} - \frac{\pi f^2}{f_{sw}}\right) \quad (18)$$

The total MMC losses, P_l, are the sum of the conduction and switching losses:

This article has been accepted for publication in a future issue of this journal, but has not been fully edited. Content may change prior to final publication. Citation information: DOI 10.1109/TPEL.2016.2557579, IEEE Transactions on Power Electronics

$$P_l = P_c + P_{sw} \approx$$
$$\approx 2v_{cell} I_m \left(\frac{3f_{sw}}{\pi} - \frac{\pi f^2}{f_{sw}} \right)(t_{on} + t_{off}) + \frac{3}{4} n I_m^2 R_{ds,on} \quad (19)$$

V. Simulation Results

In order to assess the suitability of MMCs as traction converters, the MMC efficiency has been compared with a traditional two-level IGBT inverter. Losses due to cell balancing are not considered for the two-level inverter and are instead included in the MMC, although this leads to a penalisation of the MMC in the comparison. Both converters are driven by THI-SPWM strategy and connected to a 220 V, 250 A, 50 Hz, 80 kW machine. Equal semiconductor ratings were applied for both converter types using FZ300R12KE3G IGBT [18] for the two-level inverter and AUIRFS8409-7P power MosFET [19] for the MMC. According to the technical literature, the conduction and switching losses of an IGBT-based two-level inverter are given by [20]:

$$P_{c,inverter} = \frac{3}{\pi} I_m (V_{ce,0} + V_{f,0}) + \frac{3}{4} I_m^2 (R_c + R_d) +$$
$$+ \frac{3}{4} (V_{ce,0} - V_{f,0}) I_m m \cos(\varphi) + \frac{2}{\pi} (R_c - R_d) I_m^2 m \cos(\varphi);$$
$$P_{sw,inverter} = \frac{6}{T} \sum_{l=1}^{p} E_{IGBT,on}(i_l) + E_{IGBT,off}(i_l) + E_{Diode,rec}(i_l); \quad (20)$$
$$i_l = \left| I_m \sin\left(\frac{2\pi l}{z} \right) \right|.$$

The definition of the symbols and their corresponding values for the numerical simulations are reported in Table II. $E_{IGBT,on}$ and $E_{IGBT,off}$ are given in the data sheet and can be described as a polynomial function of current i_l. Furthermore, Table II summarizes the main data of the two-level inverter and MMC parameters used for simulation.

Fig. 4 shows the 'gear changing' of the switching frequency, f_{sw}, with the fundamental frequency of the voltage output. At low speeds where the effect of the difference in the number of carrier cycles per each modulation cycle is small, asynchronous operation of the carrier frequency is applied. At moderate and high speeds, the carrier signals and the modulating wave are synchronized and the modulation frequency decreases in steps as the frequency increases to keep their ration as a whole number [21].

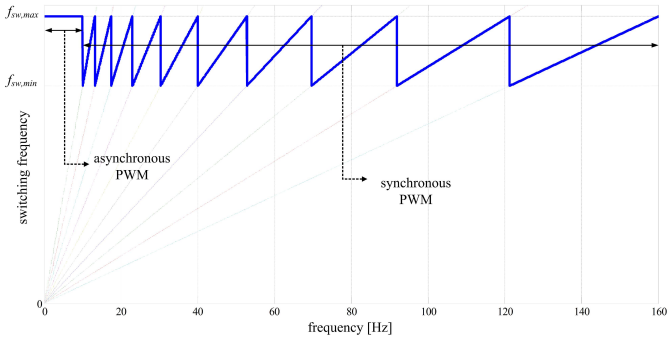

Fig. 4: Illustration of the 'gear changing' in SPWM.

Fig. 5 shows the efficiency for both topologies versus frequency when the motor is drawing half of the nominal current. Both converters are operated at a maximum switching frequency of 2 kHz and 20 kHz. It is evident that for the MMC the efficiency slightly changes with the maximum switching frequency. At maximum switching frequency of 20 kHz, the MMC efficiency is higher than the inverter efficiency by 3-5% in the constant torque region, and by 0.5-1% in the constant power region. At maximum switching frequency of 2 kHz, the MMC efficiency is lower than the inverter efficiency by 1-4% in the constant torque region, and by 1% in the constant power region.

Fig. 6 shows the efficiency for both topologies versus frequency when the motor is drawing the nominal current with the same maximum switching frequencies of the previous example. At maximum switching frequency of 20 kHz, the MMC efficiency is lower than the inverter efficiency by 1-4% in the constant torque region, and by 1-2% in the constant power region. At maximum switching frequency of 2 kHz, the MMC efficiency is lower than the inverter efficiency by 3-12% in the constant torque region, and by 3% in the constant power region. It can be also noticed that the efficiency of the MMC increases when the load current decreases; conversely, the efficiency of the two-level inverter increases when the current increases. This

TABLE II
MAIN DATA OF THE SIMULATED CONVERTERS.

	Variable	Description	Values
2-level inverter	$V_{ce,0}$	IGBT on-state zero-current collector-emitter voltage	0.921057 [V]
	R_c	IGBT collector-emitter on-state resistance	3.59 [mΩ]
	$E_{IGBT,on}$	IGBT turn-on energy	$5.3\times10^{-3} + 2.9\times10^{-5}\, i_l + 1.2\times10^{-7}\, i_l^2$ [J]
	$E_{IGBT,off}$	IGBT turn-off energy	$2.4\times10^{-3} + 1.4\times10^{-4}\, i_l$ [J]
	$V_{f,0}$	Diode on-state zero-current forward voltage	1.03562 [V]
	R_d	Diode forward on-state resistance	2.09 [mΩ]
	$E_{Diode,rec}$	Diode recovery energy	$6.8\times10^{-3} + 9.1\times10^{-5}\, i_l - 9.1\times10^{-8}\, i_l^2$ [J]
MMC	n	Number of SMs/arm	84
	v_{cell}	Cell voltage	3.2-4.2 [V]
	L	Arm inductor	50 [μH]
	$R_{ds,on}$	MosFET drain-source on-state resistance	0.55 [mΩ]
	t_{ri}	MosFET current rise time	43 [ns]
	t_{fi}	MosFET current fall time	72 [ns]
	t_{rv}	MosFET voltage rise time	0.85 [ns]
	t_{fv}	MosFET voltage fall time	6.24 [ns]

This article has been accepted for publication in a future issue of this journal, but has not been fully edited. Content may change prior to final publication. Citation information: DOI 10.1109/TPEL.2016.2557579, IEEE Transactions on Power Electronics

reflects the fact that conduction losses changes with the load and are prevalent for the MMC; switching losses do not change substantially with the load and are prevalent for the two-level inverter.

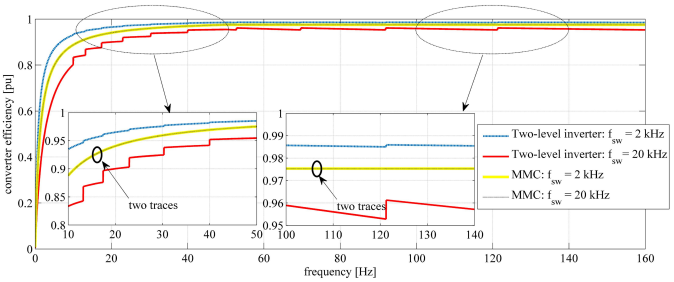

Fig. 5: The efficiency for both topologies versus frequency at half full-load current.

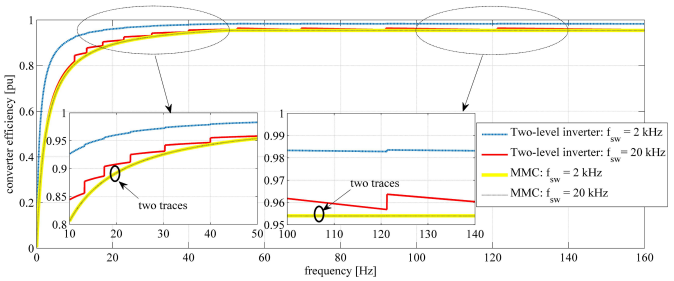

Fig. 6: The efficiency for both topologies versus frequency at full-load current.

Subsequently, the proposed control scheme for the MMC has been tested in simulation by Matlab/Simulink and compared with the two-level inverter. The data for the BEV are taken from an existing electric car (Nissan Leaf) [22]. In this simulation, the MMC has 84 Li-ion cells (4.2 V / 12.8 Ah) per arm, with a maximum line voltage of 220 V rms. The initial imbalance of the SOC of the cells has been assumed equal to 30%. The battery cells have been modelled by a parameterized dynamic model to take into account the variation of the voltage with the SOC and the current [23]:

$$\begin{aligned} V_{dis} &= E_0 - Ri - K\frac{Q}{Q-q(t)}i^* - \\ &- K\frac{Q}{Q-q(t)}q(t) + Ae^{-Bq(t)}; \qquad i^* > 0; \\ V_{ch} &= E_0 - Ri - K\frac{Q}{0.1Q+q(t)}i^* - \\ &- K\frac{Q}{Q-q(t)}q(t) + Ae^{-Bq(t)}; \quad i^* < 0, \end{aligned} \tag{21}$$

where all quantities are defined in Table III.

The data of the simulated Li-ion cell is also given in Table III. In this simulation, the load torque of the machine is given by a load-speed curve as shown in (26) [24].

$$T_L = d_1\omega_r + d_2\omega_r^2 + d_3\omega_r^3 + J_{eq}\frac{d\omega_r}{dt} \tag{22}$$

where d_1, d_2, d_3 are calculated from the load characteristics and J_{eq} is the equivalent vehicle inertia referred to the machine shaft.

The main data of the simulated vehicle and motor are reported in Table IV.

TABLE III
EXPLANATION OF QUANTITIES OF (20) AND THE DATA OF SIMULATED LI-ION CELL

V_{dis}	Battery voltage during discharge process in [V]	
V_{ch}	Battery voltage during charge process in [V]	
E_0	Battery constant voltage	4.0252 V
R	Battery internal resistance	0.14375 mΩ
i	Battery current in [A]	
K	Polarization constant	0.00026633 V/Ah
$q(t)$	Extracted capacity in [Ah]	
i^*	Low frequency current dynamics in [A]	
A	Exponential zone amplitude	0.29595 V
B	Exponential zone time constant inverse	4.7445 Ah^{-1}

TABLE IV
MAIN DATA OF THE SIMULATED VEHICLE AND MOTOR.

Transmission ratio	7.94:1
Battery capacity	24 kWh
Wheelbase	2.7 m
Curb weight	1525 kg
Maximum vehicle speed	143 km/h
Nominal motor power	80 kW
Nominal motor voltage	220 V
Machine pole pairs	1
Nominal motor speed	2730 rpm
Nominal motor current	260 A
Nominal motor electric frequency	50 Hz

The New European Driving Cycle (NEDC) has been used as the reference speed cycle for the electric vehicle. It combines the Urban Driving Cycle (UDC) repeated four consecutive times and the Extra-Urban Driving Cycle (EUDC) with maximum speed of 120 km/h. Fig. 7 shows the motor phase voltages, phase currents, and converter circulating currents during acceleration, cruising and deceleration of the car. The figure shows that the motor starts up from standstill without producing any overvoltage or overcurrent and the MMC drives the motor at low speed without exceeding the nominal current. The circulating currents are dependent on the energy arm/leg unbalancing of converter. Since the converter legs and arms have different initial energies, the arm balance controller injects the dc and fundamental components to the circulating currents to achieve the balancing within the phases and the arms. At steady-state (t = 289.5 s), the battery cells are all balanced, and the injected circulating currents are close to zero. It is worth noting that the load currents are always balanced and almost sinusoidal regardless of the SOC of the cells.
The dynamic of the SOC of all battery cells are reported in Fig. 8 to show the action of the balancing controller. In the first part of the cycle, the cells with higher SOC discharge faster, while

This article has been accepted for publication in a future issue of this journal, but has not been fully edited. Content may change prior to final publication. Citation information: DOI 10.1109/TPEL.2016.2557579, IEEE Transactions on Power Electronics

the cells with lower SOC are recharged until all the cells have very similar SOC and all the cells are completely balanced after 670 seconds. Fig. 8 also shows the reference and actual motor speeds, demonstrating the good speed control obtained with the MMC for the whole frequency range.

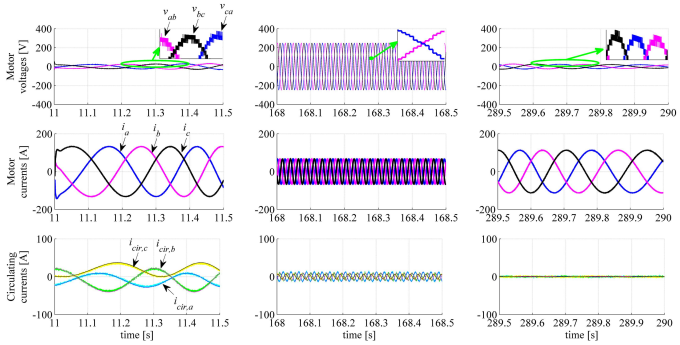

Fig. 7: The motor line voltages and currents, and the converter circulating currents.

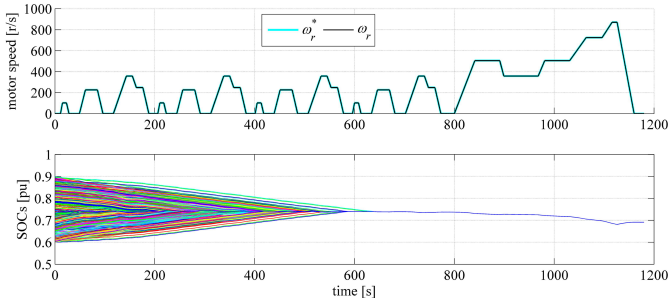

Fig. 8: The motor speed and SOCs of battery cells.

The results shown in Fig. 9 from top to bottom are the motor electric frequency, active power, the rms value of motor voltage and current, respectively. The data of Fig. 9 has been used to estimate the converter efficiency for the both topologies, MMC and the two-level inverter.

Using (18) and the data given in Fig. 9, the switching and conductions losses are calculated for the UDC and EUDC to obtain the converter efficiencies of both topologies, as shown in Fig. 10. It is interesting to note that for these cycles the MMC efficiency is most of the time higher than that of the two-level inverter. This is because the selected car never absorbs the full load current to follow the cycles and, according to theory, the MMC is advantaged at light loads. As also expected from theory, the MMC has switching losses lower than those of the two-level inverter. This is because MosFETs have lower rise and fall times than those of IGBTs and the switching losses of the MMC are independent on the number of SMs per arm. In fact, the total number of PWM pulses for all SMs of a MMC arm is equal to the total number of PWM pulses for one device of the two-level inverter. On the other side, the MMC has conduction losses higher than those of the two-level inverter, because they linearly depend on the number of SMs of each arm.

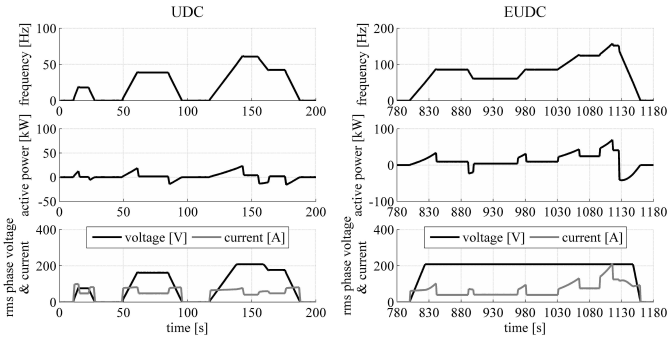

Fig. 9: The motor electric active power, voltage and current.

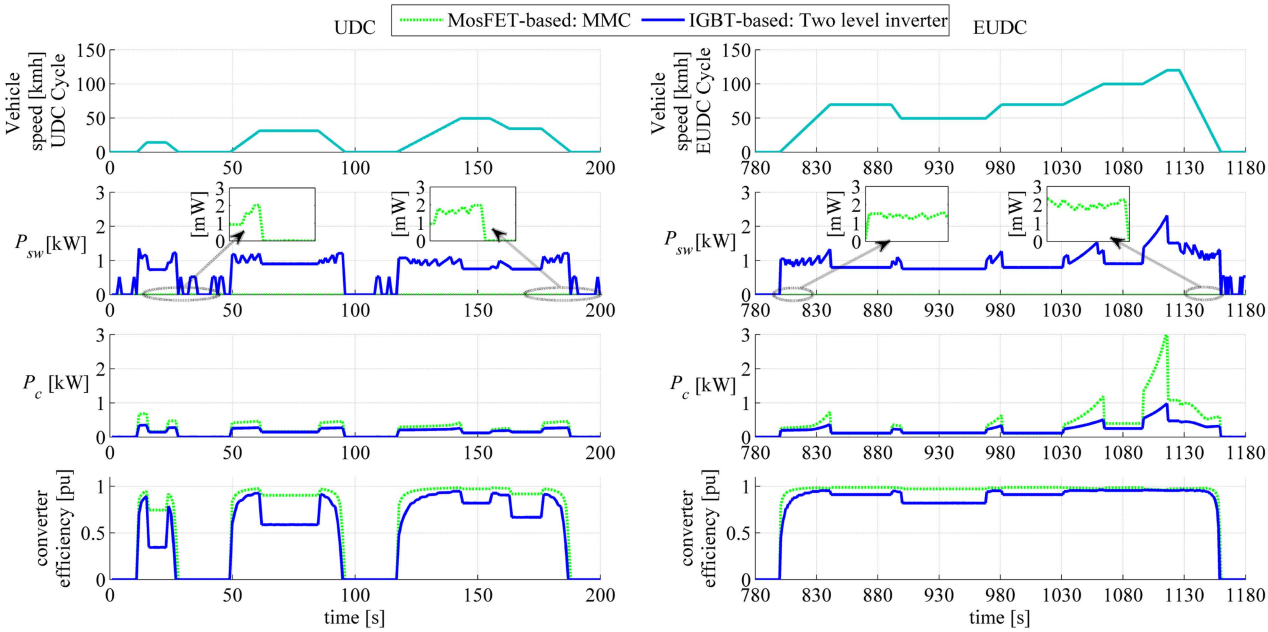

Fig. 10: The converter switching losses, conduction losses, and efficiency.

This article has been accepted for publication in a future issue of this journal, but has not been fully edited. Content may change prior to final publication. Citation information: DOI 10.1109/TPEL.2016.2557579, IEEE Transactions on Power Electronics

VI. EXPERIMENTAL RESULTS

The capabilities of following the NEDC and the model for the calculation of losses have been experimentally verified with a prototype of MMC with 4 SMs per arm, whose photograph is shown in Fig. 11. Each SM includes a lithium-ion cell with 3.7 V and 10 Ah capacity. The control system is based on a NI CompactRIO, which combines an embedded real-time processor, a high-performance FPGA, and hot-swappable I/O modules.

The induction motor used for the experiments has the data given in Table V . A 10V / 400V, 1.2 kVA three-phase transformer has been used to boost the converter voltage to the level suitable for the motor. Table V also summarizes the circuit and battery parameters used for experiment. The 24 Li-ion cells have been charged to different initial SOC values in order to test the SOC control; the maximum SOC unbalancing between the cells has been set to be around 40%.

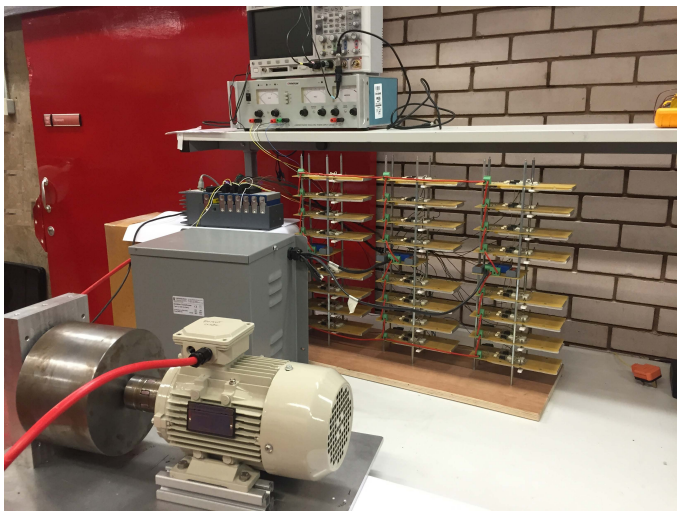

Fig. 11: Prototype of a 5-level MMC with embedded lithium-ion batteries.

TABLE V
MOTOR ELECTRIC DATA AND THE CONVERTER PARAMETERS USED FOR EXPERIMENT

Nominal motor power	0.55 kW
Nominal motor voltage	400 V
Nominal motor electric frequency	50 Hz
Nominal motor current	1.34 A
Nominal motor Speed	1435 rpm
Pole Pairs	2
Number of SMs/arm	4
MosFET drain-source on-state resistance	0.8 mΩ
MosFET current rise time	240 ns
MosFET current fall time	93 ns
Nominal converter voltage	10 V
Nominal converter current	50 A
Maximum switching frequency	2 kHz
Minimum switching frequency	1.2 kHz
Arm inductor	22 µH

The results shown in Fig. 12 from top to bottom are the motor reference speed and the measured motor speed, and the SOCs of all the battery cells. The traction control tracks the reference speed accurately and the SOCs of all the battery cells converge toward the same level in about 2,500 seconds. This is in agreement with the simulation result, since the converter nominal current used for experiment is about 5 times smaller than that used for the simulations.

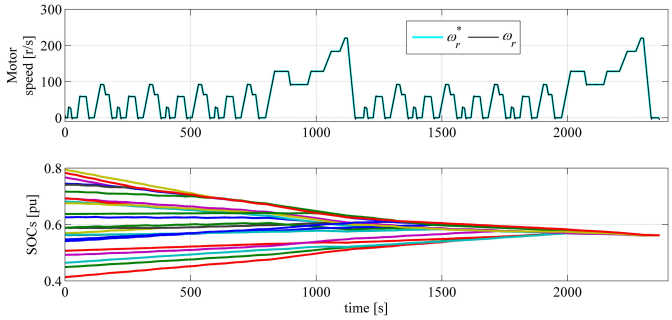

Fig. 12: The motor speed, and SOCs of battery cells.

To validate the calculation efficiency of the proposed MMC, the switching and conduction losses have been measured for one SM at different motor speeds during the whole NEDC. For this experiment, all battery cells have been charged to the same initial SOC value. In this case, the estimated efficiency of one SM is approximately equal to the MMC efficiency, since the converter has equal SMs. The drain-source on-state resistance for the power MosFET of the prototype is 1 mΩ. The experimental switching process of one power MosFET is presented in Fig. 13, where the top figure presents the drain-source voltage and the drain current and the bottom figure shows the power losses, with a qualitative separation into conduction and switching losses.

Fig. 14 shows the converter output phase voltage and current, the SM instantaneous input power, and the corresponding instantaneous power losses at different motor speeds. The waveforms of voltage and current shows that the MMC prototype produces phase currents with a very small THD, even with only 4 SMs per arm.

TABLE VI
POWER OF THE BATTERY CELLS, POWER LOSSES, AND EFFICIENCY OF ONE SM

Electric frequency [Hz]	Battery cell power [W]	Power losses of one SM [W]	Experimental efficiency of one SM [%]	Simulated efficiency of one SM [%]
10.89	19.00	4.19	77.95	78.85
16.99	15.60	2.42	84.49	85.14
32.46	15.33	2.52	83.35	84.98
49.06	12.11	2.32	80.84	82.04
66.23	12.96	2.15	83.41	84.53

This article has been accepted for publication in a future issue of this journal, but has not been fully edited. Content may change prior to final publication. Citation information: DOI 10.1109/TPEL.2016.2557579, IEEE Transactions on Power Electronics

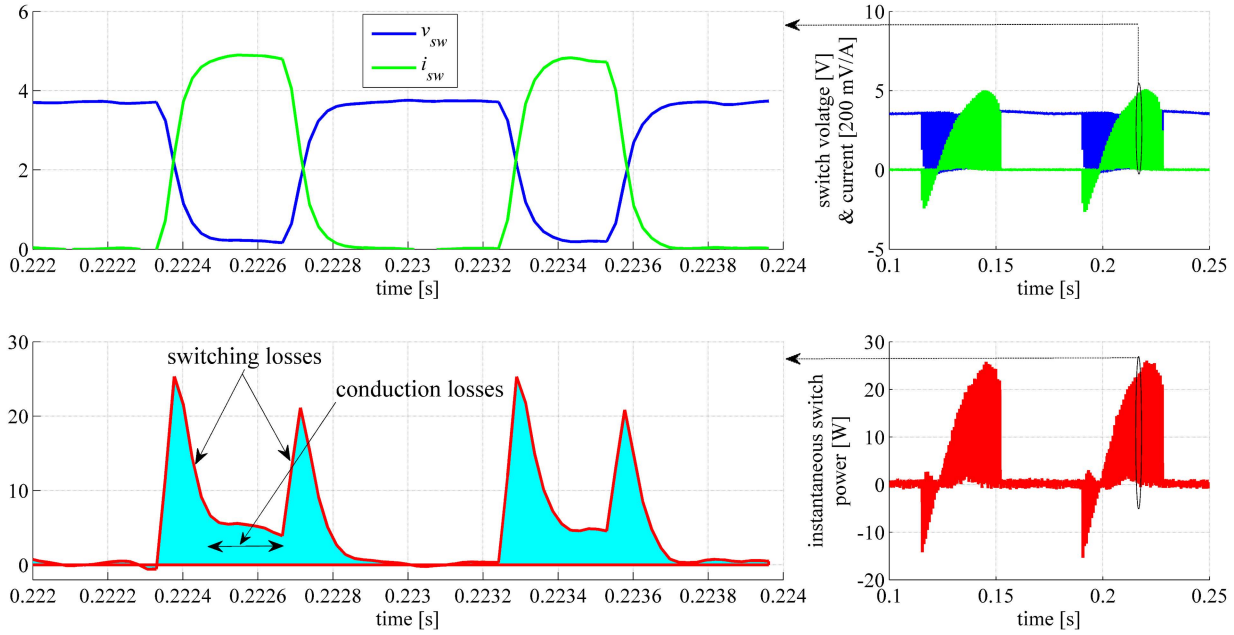

Fig. 13: Experimental curves of the switching process of one power MosFET.

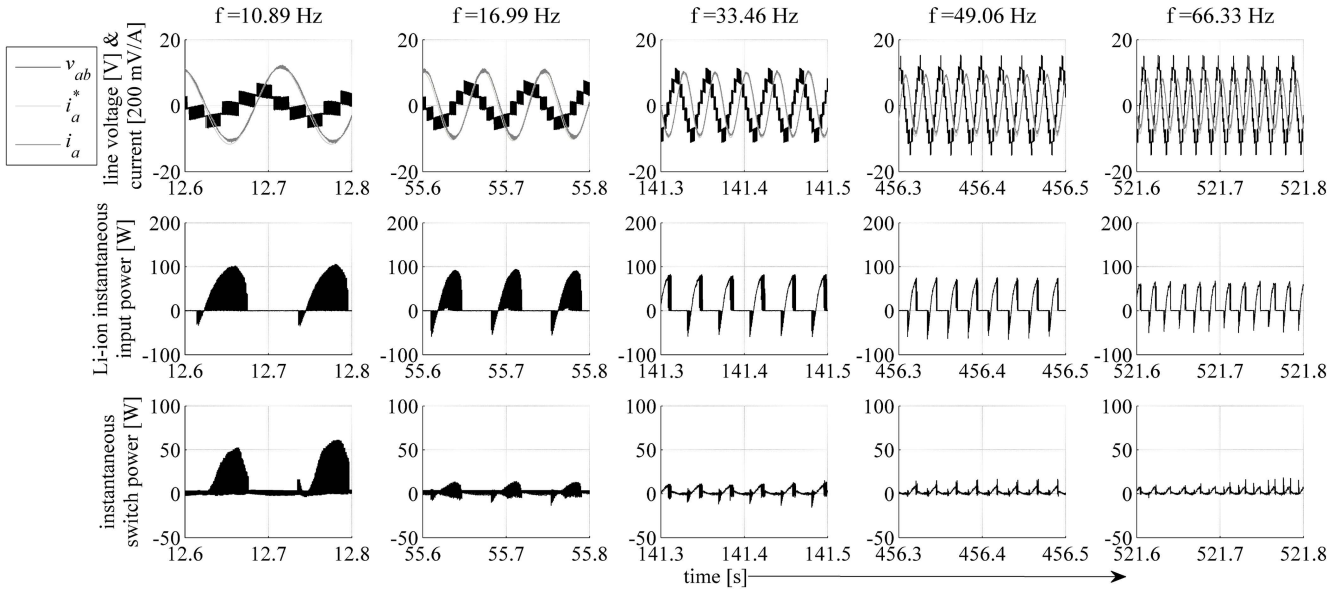

Fig. 14: Phase voltage and current, instantaneous battery cell power, and SM instantaneous losses at different motor speeds.

The experimental efficiency of a SM has been also compared with the simulations carried out for the same number of SMs. The result of this comparison is shown in Table VI that includes also the average power of the battery cells and the average power losses. Both simulated and experimental efficiencies at different motor speeds show a close agreement, with a difference of 1-2 %, due to the additional dead-time losses of the experimental setup.

VII. Conclusion

This paper presents a detailed assessment of the performance of modular multilevel converters with integrated battery cells for the traction drive of electric vehicles. This topology integrates the battery management system in the power converter, without the need of external balancing circuits. The state of charge of the battery cells is balanced by the arm and cell balancing controllers that do not affect the waveforms of the motor current. The proposed converter produces an extremely low distortion of the motor current, with direct benefits on the motor efficiency. An analytical method for the calculation of power losses of the proposed modular multilevel converter has been also presented and has been verified by numerical simulations and experiments. The losses of the proposed converter has been compared with those of traditional two-level converters and have shown that the proposed converter presents better efficiencies at light loads, since losses

are predominantly given by conduction losses. This suggests that proposed converter is preferred for urban use of electric car, where the motor is mostly used below its full power. The proposed converter has been also tested with simulations and experiments to balance the battery cells and follow the new European driving cycle, showing a balancing time of 670 seconds for a 30% imbalance and good capabilities of tracking the reference speed even during cell balancing.

APPENDIX A1 - DERIVATION OF REFERENCE AC CIRCULATING CURRENTS

The zero sequence of the reference circulating currents has to be eliminated by adjusting $i_{m,cir,k}$ and γ_k.

$$i_{m,cir,a}\sin(\omega t+\gamma_a)+i_{m,cir,b}\sin(\omega t+\gamma_b-2\pi/3)+ \\ +i_{m,cir,c}\sin(\omega t+\gamma_c+2\pi/3)=0. \tag{A1.1}$$

Using trigonometric identities, (A1.1) can be re-written as:

$$\begin{aligned} &i_{m,cir,a}\sin(\gamma_a)+i_{m,cir,b}\sin(\gamma_b-2\pi/3)+ \\ &+i_{m,cir,c}\sin(\gamma_c+2\pi/3)=0. \\ &i_{m,cir,a}\cos(\gamma_a)+i_{m,cir,b}\cos(\gamma_b-2\pi/3)+ \\ &+i_{m,cir,c}\cos(\gamma_c+2\pi/3)=0. \end{aligned} \tag{A1.2}$$

Recalling the output of the differential energy balance controller:

$$i_{m,cir,k}\cos\gamma_k=c_k. \tag{A1.3}$$

To simplify the computational time, the circulating current phase γ_a, has been set to zero and then, solving for γ_b, γ_c, $i_{mcir,a}$, $i_{mcir,b}$, and $i_{mcir,c}$:

$$\gamma_b=\tan^{-1}\left(\frac{c_a+c_b-2c_c}{\sqrt{3}c_c}\right);\quad \gamma_c=-\tan^{-1}\left(\frac{c_a-2c_b+c_c}{\sqrt{3}c_b}\right); \\ i_{m,cir,a}=c_a;\quad i_{m,cir,b}=\frac{c_b}{\cos(\gamma_b)};\quad i_{m,cir,c}=\frac{c_c}{\cos(\gamma_c)}. \tag{A1.4}$$

APPENDIX A2 – DISCRETE TIME CALCULATING CURRENT CONTROLLER

From (5), the block diagram of the energy-based control structure in the discrete-time domain is presented in Fig. 15, in which the phase-energy and arm-energy controls are combined with a circulating current control. The closed loop transfer functions can be represented as:

$$\begin{aligned} &\overline{\mathrm{SOC}}_k(z)=K_1\frac{(z+1)(z-\alpha_1)}{a_1z^2+b_1z+c_1}\overline{\mathrm{SOC}}_k(z)- \\ &-K_2\frac{(z+1)(z-1)}{a_2z^2+b_2z+c_2}\mathrm{D}(z) \\ &\frac{\overline{\mathrm{SOC}}_{kt}(z)-\overline{\mathrm{SOC}}_{kb}(z)}{\overline{\mathrm{SOC}}^*_{kt}(z)-\overline{\mathrm{SOC}}^*_{kb}(z)}=K_3\frac{(z+1)(z-\alpha_3)}{a_3z^2+b_3z+c_3} \\ &\frac{I_{cir,k}(z)}{I^*_{cir,k}(z)}=K_4\frac{z+1}{z+c_4} \end{aligned} \tag{A2.1}$$

where T_s denotes the sampling period of the digital system, $\mathrm{D}(z) = 0.5I_mV_m\cos(\varphi)$, and the relation between the parameters given in (A2.1) and the control gains are:

$$K_1=\frac{k_1}{T_sQ}+\frac{k_2}{2Q};\quad K_2=\frac{1}{T_sQ}; \\ K_3=-\frac{mk_3}{T_sQ}-\frac{mk_4}{2Q};\quad K_4=\frac{T_sk_5}{2L}. \tag{A2.2}$$

$$a_1=a_2=\frac{k_1}{T_sQ}+\frac{k_2}{2Q}+\frac{4}{T_s^2}; \\ a_3=-\frac{mk_3}{T_sQ}-\frac{mk_4}{2Q}+\frac{4}{T_s^2}. \tag{A2.3}$$

$$b_1=b_2=\frac{k_2}{Q}-\frac{8}{T_s^2}; \\ b_3=-\frac{mk_4}{Q}-\frac{8}{T_s^2}. \tag{A2.4}$$

$$c_1=c_2=-\frac{k_1}{T_sQ}+\frac{k_2}{2Q}+\frac{4}{T_s^2}; \\ c_3=\frac{mk_3}{T_sQ}-\frac{mk_4}{2Q}+\frac{4}{T_s^2}; \\ c_4=\frac{T_sk_5}{2L}-1. \tag{A2.5}$$

$$\alpha_1=\frac{2k_1-T_sk_2}{2k_1+T_sk_2}; \\ \alpha_2=\frac{2k_3-T_sk_4}{2k_3+T_sk_4}. \tag{A2.6}$$

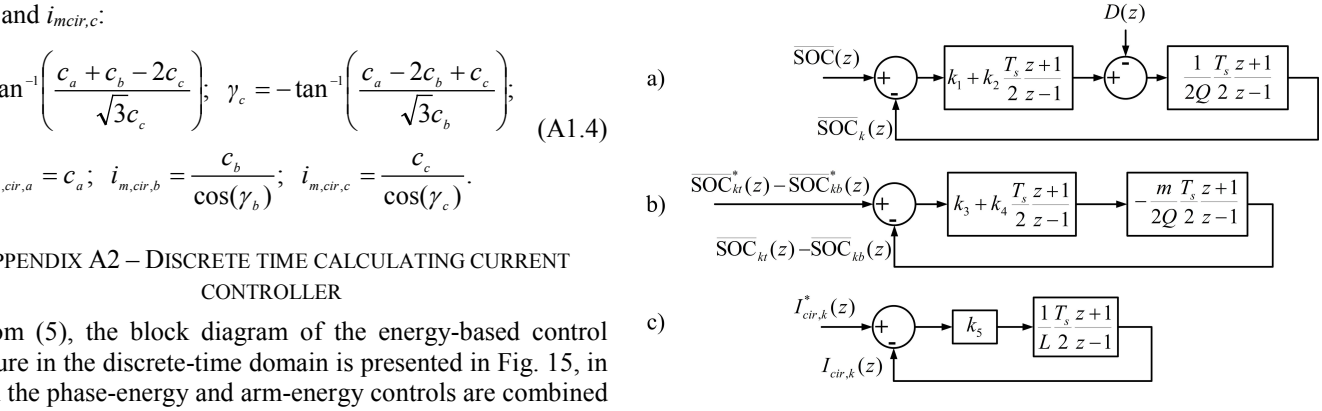

Fig. 15: a) Leg-energy balance control system. b) Arm-energy balance control system. c) Circulating current control system.

REFERENCES

[1] J. Yun, T. Yeo, and J. Park, "High Efficiency Active Cell Balancing Circuit with Soft Switching Technique for Series-Connected Battery String", in *Proc. of Twenty-Eighth IEEE Applied Power Electron. Conf. and Exp. (APEC)*, pp. 3301-3004, Long Beach, CA, 17-21 Mar. 2013.

[2] J. Kim, J. Shin, C. Chun, and B.H. Cho, "Stable Configuration of a Li-Ion Series Battery Pack Based on a Screening Process for Improved Voltage/SOC Balancing", *IEEE Trans. Power Electron.*, vol. 27, no. 1, pp. 411-424, 2 Jun. 2012.

[3] S. D'Arco, L. Piegari, and P. Tricoli, "A modular converter with embedded battery cell balancing for electric vehicles", in *Proc. Electr. Sys. Aircraft, Railway and Ship Propulsion ESARS 2012*, pp. 1-6, Bologna, Italy, 16-18 Oct. 2012.

[4] S. D'Arco, L. Piegari, and P. Tricoli, "Power and balancing control considerations on modular multilevel converters for battery electric vehicles," in *Proc. 15th European Conf. on Power Electron. and Applicat. (EPE)*, pp.1,9, 2-6 Sept. 2013.

[5] S. D'Arco, L. Piegari, M. S. Quraan, and P. Tricoli, "Battery charging for electric vehicles with modular multilevel traction drives," in *Proc. 7th IET Int. Conf. on Power Electron., Mach. and Drives (PEMD 2014)*, pp.1,6, 8-10 April 2014.

[6] S. Jiang, L. Qi, X. Cui, and P. Wang, "Impact analysis of practical factors for an equivalent model of modular multilevel converter," in *Proc. Power System Technology (POWERCON), 2014 Int. Conf. on*, vol., no., pp.2228-2235, 20-22 Oct. 2014.

[7] X. Liu, A. Lindemann, and H. Amiri, "Theoretical and experimental comparison of different control strategies for modular multilevel converters," in *Proc. Control and Modeling for Power Electron. (COMPEL), 2014 IEEE 15th Workshop on*, vol., no., pp.1-9, 22-25 June 2014.

[8] M. Quraan, T. Yeo, and P. Tricoli, "Design and control of modular multilevel converters for battery electric vehicles", *IEEE Trans. Power Electron.*, vol. 31, no. 1, pp. 507-515, Jan. 2016.

[9] H. Akagi, "Classification, terminology, and application of the modular multilevel cascade converter (MMCC)", *IEEE Trans. Power Electron.,* vol. 26, no. 11, pp. 3119-3130, Nov. 2011.

[10] P.M. Meshram and V.B. Borghate, "A Simplified Nearest Level Control (NLC) Voltage Balancing Method for Modular Multilevel Converter (MMC)", *IEEE Trans. Power Electron.*, vol. 30, no. 1, pp. 450-462, 2 Jan. 2015.

[11] G.S. Konstantinou, M. Ciobotaru , and V.G. Agelidis, "Operation of a modular multilevel converter with selective harmonic elimination PWM", in *Proc. IEEE 8th Int. conf. on Power Electron. and ECCE Asia (ICPE and ECCE)*, pp. 999-1004, Jeju, Korea, 2011.

[12] R. Zeng, L. Xu, L. Yao, and B.W. Williams, "Design and operation of a hybrid modular multilevel converter", *IEEE Trans. Power Electron.*, vol. 30, no. 3, pp. 1137-1146, 29 April 2014.

[13] Y. Zhang, G.P. Adam, T.C. Lim, S.J Finney, and B.W. Williams, "Analysis of modular multilevel converter capacitor voltage balancing based on phase voltage redundant states", *IET Power Electron.*, vol. 5, no. 6, pp. 726-738, Jul. 2012.

[14] L. Maharjan, S. Inoue, H. Akagi, and J. Asakura, "State-of-charge (SOC)-balancing control of a battery energy storage system based on a cascade PWM converter", *IEEE Trans. Power Electron.*, vol. 24, no. 6, pp. 1628-1636, Jun. 2009.

[15] D.J. Deepti, and V. Ramanarayanan, "State of charge of lead acid battery", in *Proc. India Int. Conf. Power Electron.*, pp. 89-93, Chennai, India, 19-21 Dec. 2006.

[16] A. Lesnicar, and R. Marquardt, "An innovative modular multilevel converter topology suitable for a wide power range", in *Proc. IEEE Bologna Power Tech. Conf.* ,vol. 3, pp. 1-6, Bologna, Italy, 23-26 Jun. 2003.

[17] M.H. Rashid, "The Power MOSFET," in Power Electronics Circuits, Drives and Applications," 3rd ed., Upper Saddle River, USA, 4 Aug. 2003.

[18] Infineon, "IGBT-Module," FZ300R12KE3G datasheet, Oct. 2013.

[19] International Rectifier, "HEXFET Power MOSFET," AUIRFS8409-7P datasheet, Apr. 2013.

[20] M. H. Bierhoff, and F. W. Fuchs, "Semiconductor losses in voltage source and current source IGBT converters based on analytical derivation", in *Proc. Power Electron. Specialists Conf., 2004. PESC 04. 2004 35th Annu.*, vol. 4, pp. 2836-2842, 2004.

[21] D. W. Novotny and T. A. Lipo, "The Pulse Width Modulated Inverter," in Vector control and Dynamics of AC Drive," 1st ed., New York, USA, 25 Jul. 1996.

[22] Carinf, "Nissan Leaf ZE0 (2010) - technical specifications," carinf.com, 2010. [Online]. Available: http://www.carinf.com/en/9e60422878.html. [Accessed Aug. 24, 2015].

[23] O. Tremblay, and L.A. Dessaint, "Experimental validation of a battery dynamic model for EV applications" World Electric Vehicle Journal, vol. 3, May 2009.

[24] P. Tricoli and E. Pagano, "controllo di velocita e posizione dei motori elettrici," in Nozioni complementari di macchine ed azionamenti elettrici," 1st ed., Italy, 1 Jan. 2010.

Mahran Quraan received the B.Sc. degree in electrical engineering from Birzeit University, Palestine, in 2008, and the M.Sc. degree in electrical power engineering from the University of Strathclyde, Glasgow, UK, in 2012, under a full scholarship from the "Palestinian Student Scholarship Scheme." He is currently working toward the Ph.D. degree at the School of Electronic, Electrical, and Systems Engineering, University of Birmingham, Birmingham, U.K., with a scholarship funded by Palestinian Telecommunication Group (PalTel), Samsung Advanced Institute of Technology, and the University of Birmingham. He subsequently worked as a Teaching and Research Assistant in the Department of Electrical Engineering, Birzeit University. He then joined the Department of Electrical Engineering, Birzeit University, as a Faculty Member. His research interests include modular multilevel converters, battery management systems, protection and control of power systems, control of power converters, and ac machine drives.

Pietro Tricoli (M'06) was born in Naples, Italy, on September 8, 1978. He received the M.S. (*cum laude*) and Ph.D. degrees in electrical engineering from the University of Naples Federico II, Italy, in 2002 and 2005, respectively.

He was a Visiting Scholar in the Department of Electrical and Computer Engineering, University of Wisconsin-Madison, Madison, in 2005. In 2006, he was also a Visiting Scholar in the Department of Electrical and Electronic Engineering, Nagasaki University, Nagasaki, Japan. From 2006 to 2011, he was a Postdoctoral Research Fellow with the Department of Electrical Engineering, University of Naples Federico II, Italy. He is currently a Lecturer of Electrical Power and Control in the School of Electronic, Electrical, and Systems Engineering, University of Birmingham, Birmingham, U.K. He is the author of more than 60 scientific papers published in international journals and conference proceedings. His research interests include the modelling of storage devices for road electric vehicles, railways, and rapid transit systems, the wind and photovoltaic generation, and the modeling and control of multilevel converters.

Dr. Tricoli is a member of the IEEE Industrial Electronics Society. He is the Web & Publication Chair of the International Conference on Clean Electrical Power. He is a Registered Professional Engineer in Italy.

Salvatore D'Arco received the M.Sc. and Ph.D. degrees in electrical engineering from the University of Naples Federico II, Naples, Italy, in 2002 and 2005, respectively. From 2006 to 2007, he was a Postdoctoral Researcher with the University of South Carolina, Columbia, SC, USA. In 2008, he joined ASML Holding N.V., Veldhoven, The Netherlands, where he worked as a Power Electronics Designer until 2010. From 2010 to 2012, he was a Postdoctoral Researcher with the Department of Electric Power Engineering, Faculty of Information Technology, Mathematics and Electrical Engineering, Norwegian University of Science and Technology, Trondheim, Norway. In 2012, he joined SINTEF Energy Research, Trondheim, Norway, where he currently works as a Research Scientist. He is the author of over 50 scientific papers, and he is the holder of one patent. His main research activities are related to the control and analysis of power electronic conversion systems for power system applications, including the real-time simulation and rapid prototyping of converter control systems.

Luigi Piegari (M'04, SM'13) was born in 1975. He received the M.S. and Ph.D. degrees in electrical engineering from the University of Naples Federico II, Naples, Italy, in 1999 and 2003, respectively. Currently, he is an Associate Professor of Electrical Machine, Drives and Power Electronics at DEIB, Politecnico di Milano, Milan, Italy. His current research interests include electrical machines, high-efficiency power electronic converters, DC distribution grids, renewable energy sources and storage systems modeling.